Article | Received 23 February 2026; Revised 4 May 2026; Accepted 25 May 2026; Published 5 June 2026
https://doi.org/10.55092/ ae20260004

Development of a 3D-printed hybrid compliant revolute joint with enhanced directional stiffness

Zhengyao Wang[1], Richard Kavanagh[1], Yancheng Zhang[2] and Guangbo Hao[1,*]

[1] School of Engineering and Architecture, University College Cork, Cork, Ireland
[2] CEMEF, MINES ParisTech, PSL–Research University, Sophia Antipolis, France

* Correspondence author; E-mail: G.Hao@ucc.ie.

Highlights:

- A hybrid compliant revolute joint is proposed to enhance directional stiffness without compromising rotational compliance.
- Directional stiffness is achieved through strategic distribution of structural PLA reinforcement ribs within a compliant TPU matrix.
- Finite element analysis shows that the hybrid joint achieves a significantly higher off-axis to on-axis rotational stiffness ratio than mono-material designs.
- The design is compatible with monolithic fabrication via dual-material fused deposition modelling.

Abstract: Compliant revolute joints (CRJs) offer advantages in terms of frictionless motion, compactness, and monolithic fabrication, but their practical application is often constrained by an inherent stiffness–flexibility trade-off. High rotational compliance is typically accompanied by insufficient resistance to off-axis deformation, leading to parasitic motion and reduced directional stability. To address this challenge, this study proposes a hybrid CRJ designed to enhance directional stiffness while maintaining large elastic rotational capability. The joint integrates stiff polylactic acid (PLA) reinforcement ribs within a compliant thermoplastic polyurethane (TPU) matrix, with material distribution strategically tailored to suppress off-axis deformation without compromising the intended rotational motion. The design is compatible with monolithic fabrication via dual-material fused deposition modelling (FDM). Finite element analysis, informed by experimentally characterised material and interfacial properties, is employed to evaluate the mechanical performance of the proposed joint. The results demonstrate that the hybrid joint exhibits a significantly higher ratio of off-axis to on-axis rotational stiffness compared with mono-material PLA and TPU joints, indicating effective suppression of parasitic deformation while preserving rotational compliance.

Keywords: compliant revolute joints; hybrid-material design; off-axis to on-axis stiffness ratio; dual-material fused deposition; finite element analysis

1. Introduction

Compliant mechanisms (CMs) achieve motion, force, or energy transmission through elastic deformation of flexible members rather than through discrete rigid-body joints [1]. Compared with conventional rigid-body mechanisms assembled from multiple components connected by kinematic pairs, CMs are typically monolithic structures interconnected by flexure elements, which eliminates sliding or rolling interfaces and thereby reduces friction and backlash [2]. These characteristics enable compact, lightweight designs with high motion accuracy, and have led to the widespread adoption of CMs in applications such as articulated and continuum robotic systems, where geometric compactness and precise motion are critical [3–5].

In such applications, rotational motion is commonly realised using compliant joint (CJ) architectures based on elastic bending. When a single, dominant rotational degree of freedom (DOF) is required, compliant revolute joints (CRJs) are often preferred. Nevertheless, CRJ designs inherently inherit the stiffness–flexibility trade-off of CMs [6,7]. Increasing joint compliance facilitates large elastic rotations about the intended axis but often leads to insufficient resistance to off-axis deformation under external loading. Conversely, increasing joint stiffness improves resistance to unintended deformation modes, but restricts the achievable elastic rotation and increases mechanical resistance to motion [8]. Achieving large elastic rotational capability while maintaining adequate directional stiffness therefore remains a central challenge in CRJ design.

To address this challenge, a range of design strategies has been explored. Geometry-based approaches enhance directional stiffness through tailored joint shapes or flexural arrangements, but often do so at the expense of reduced compliance along the intended rotational axis, leading to limited off-axis to on-axis stiffness ratios [9,10]. Reinforcement-based approaches introduce locally stiff features to increase bending resistance; however, such designs frequently rely on single-material implementations or multi-part assembly, which can introduce fabrication complexity, assembly tolerances, and reduced structural consistency [11]. As a result, the development of a structurally simple, monolithic CRJ that achieves a high off-axis to on-axis rotational stiffness ratio while remaining readily manufacturable remains insufficiently addressed.

In this context, hybrid-material design offers a promising route to decouple rotational compliance from directional stiffness at the joint level. By spatially distributing stiff and compliant materials within a single joint geometry, it becomes possible to selectively enhance resistance to undesired deformation modes without compromising the intended compliant motion. Accordingly, this study proposes a hybrid CRJ fabricated via dual-material fused deposition modelling (FDM), in which stiff polylactic acid (PLA) reinforcement ribs are integrated within a compliant thermoplastic polyurethane (TPU) matrix. Through tailored material distribution, the proposed joint aims to enhance off-axis stiffness while preserving large elastic rotational compliance, providing an effective joint-level strategy for improving directional stiffness in CRJ design.

2. Design, fabrication, and evaluation methods

2.1. Design requirements

Previous CRJ designs often suffer from limited directional stiffness and excessive off-axis deformation, particularly when large elastic rotations are required. These limitations originate from the inherent stiffness–flexibility trade-off of CMs, in which increasing rotational compliance about the intended axis is frequently accompanied by reduced resistance to unintended deformation modes. To address these limitations at the joint level, the proposed CRJ is designed to satisfy the following mechanical and structural requirements:

- Large elastic rotational capability: The joint shall accommodate elastic rotations of up to ± 1.5 rad about the primary rotation axis without yielding or permanent deformation and shall fully recover its original configuration upon unloading.
- Strong directional compliance: The joint shall exhibit a high ratio of off-axis to on-axis rotational stiffness, enabling compliant motion along the intended rotational axis while effectively suppressing parasitic off-axis deformation.
- Structural simplicity and manufacturability: The joint shall maintain a compact and monolithic structure that is compatible with FDM, avoiding complex multi-part assembly or post-processing.

2.2. Conceptual structural design and hybrid material strategy

(1) Baseline joint geometry

A variety of structural configurations have been proposed for CRJs, including long single-blade flexures, notch-based hinges, and curved flexure hinges, each offering different trade-offs between flexibility and constraint capability [12–15]. Amongst these, the single-blade designs are widely employed in CRJs due to their structural simplicity and ease of fabrication, and are also commonly used as fundamental elements in more complex CRJs [16–18].

As illustrated in Figure 1a, the single-blade configuration permits three deformation modes: two in-plane motions, *i.e.*, rotation about the z-axis (Rz) and translation along the x-axis (Tx), as well as an out-of-plane motion about the y-axis (Ry). The presence of this out-of-plane motion (Ry), which constitutes an undesired off-axis deformation relative to the intended on-axis rotation about z-axis (Rz), arises from the insufficient geometric constraint inherent to the single-blade design, and may lead to reduced kinematic precision [19].

To overcome this limitation, a symmetric diamond-shaped configuration is proposed, as shown in Figure 1b. As a multi-beam compliant structure, it forms a coupled system with enhanced geometric constraints. Based on the equivalent wire-beam representations of the structures in Figure 1, the diamond-shaped configuration can be interpreted as an extension of the single-blade design with two additional folded-beam flexures, thereby introducing extra constraints. Through the kinematic compatibility of the overall structure, these added constraints significantly increase the out-of-plane stiffness to suppress the off-axis rotation (Ry), thereby enabling a more well-defined on-axis rotational behaviour about the z-axis (Rz).

Therefore, the diamond-shaped configuration is adopted in this study as a representative architecture to explore stiffness modulation via multi-material design, owing to its superior constraint capability. It should be emphasised that the focus of this work is not on geometric optimisation, but on demonstrating the feasibility and effectiveness of hybrid material strategies.

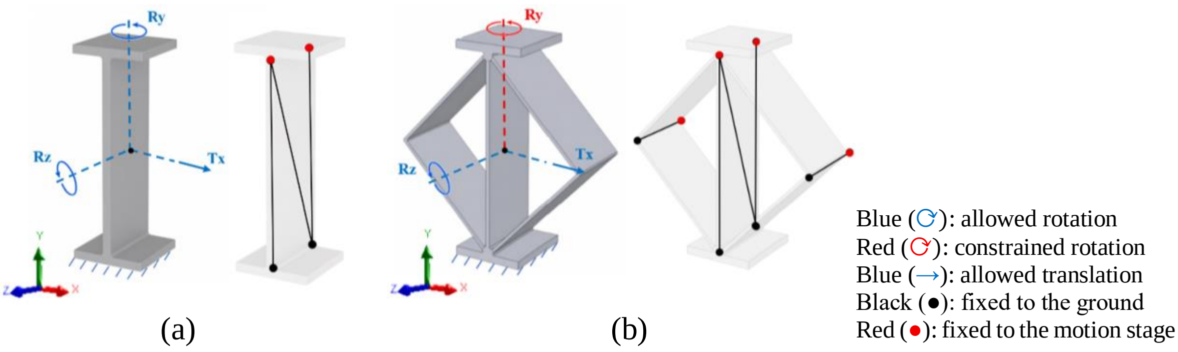

Figure 1. Comparison of CRJ configurations and their equivalent wire-beam models: **(a)** single-blade CRJ; **(b)** diamond-shaped CRJ.

(2) Hybrid material strategy for directional stiffness enhancement

Although the diamond-shaped geometry provides improved directional compliance, a mono-material implementation of this design still faces an inherent stiffness–flexibility trade-off at the joint level. The use of high-modulus materials enhances resistance to off-axis bending and torsion, but significantly reduces compliance about the intended rotational axis. Conversely, low-modulus materials permit large elastic rotations but provide insufficient resistance to off-axis deformation.

These limitations indicate that geometric tailoring alone is insufficient to decouple rotational compliance from directional stiffness. To address this challenge, a hybrid-material CRJ is proposed, as illustrated in Figure 2, with key geometric dimensions defined in Figure 3. In this design, a compliant matrix is locally reinforced by high-stiffness ribs embedded within the diamond-shaped geometry.

Inspired by the I-beam principle [20], the reinforcement ribs are positioned along the lateral edges of the joint, away from the neutral axis (NA) associated with bending in undesired directions. This material redistribution increases the second moment of area of the joint cross-section for off-axis bending, thereby enhancing directional stiffness while preserving compliance about the intended rotational axis.

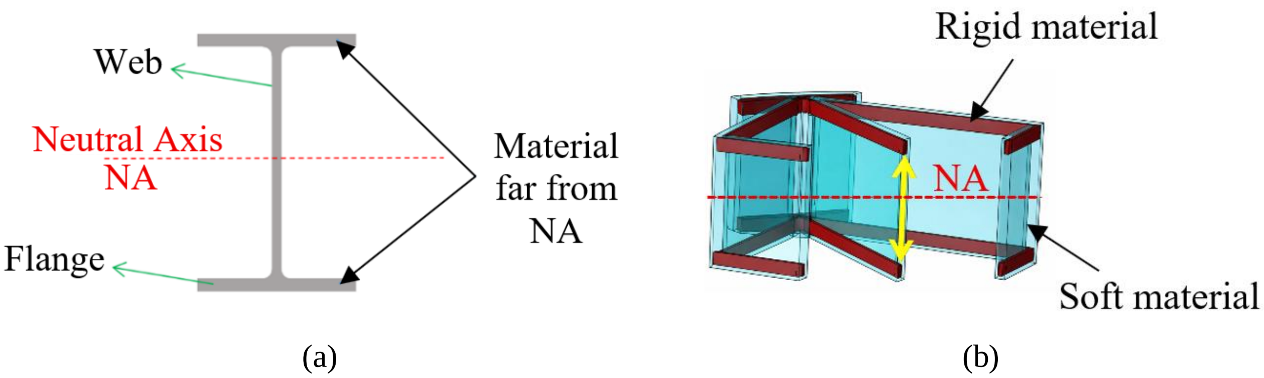

Figure 2. Schematic analogy between: **(a)** classical I-beam cross-section; **(b)** proposed hybrid CRJ with stiff reinforcement ribs positioned away from the NA.

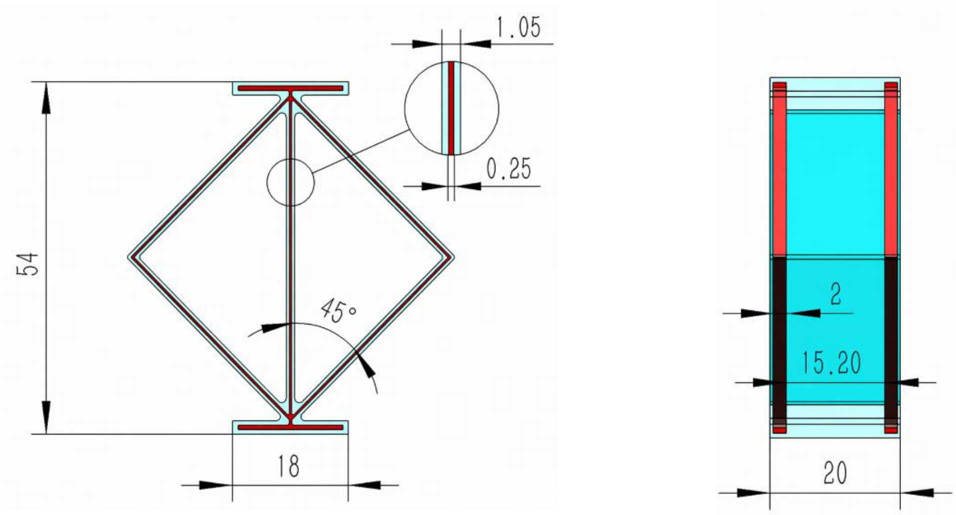

(a) (b)

Figure 3. Dimensions of the diamond-shaped hybrid CRJ: **(a)** front view; **(b)** side view (units: mm).

2.3. Material selection

Material selection for the proposed CRJ is guided by a systematic materials selection approach based on the Ashby method [21], in accordance with the hybrid material strategy for directional stiffness enhancement. Accordingly, the material selection problem is decomposed into two complementary tasks: selection of a compliant material governing on-axis rotational compliance, and selection of a stiff material for the reinforcement ribs. All selected materials are further required to minimise structural weight and be compatible with dual-material FDM, with particular consideration given to interfacial compatibility and process stability in multi-material printing.

For the compliant matrix, elastic bending dominates the deformation behaviour and directly determines the achievable rotational compliance of the joint. Two material indices were therefore established. The first index, $M_1 = \sigma_f / E$, represents the strength-to-stiffness ratio and approximates the maximum recoverable elastic strain prior to yielding. The second index, $M_2 = (E\rho)/\sigma_f^2$, penalises high stiffness and density relative to strength and is associated with minimising elastic energy storage per unit mass during deformation, which is beneficial for reducing actuation torque requirements and improving energy efficiency, where E is Young's modulus, σ_f is the yield strength, and ρ is the material density. Mapping these indices onto Ashby charts of specific strength (σ_f/ρ) *versus* specific modulus (E/ρ), generated using Ansys Granta EduPack (2024 R1), identifies elastomeric polymers as the most suitable candidates for the compliant region. Among FDM-compatible elastomers, TPU95A was selected due to its high elastic strain capacity, low density, and reliable processability.

For the reinforcement ribs, the primary requirement is high specific stiffness to enhance off-axis rigidity and resistance to compressive and bending loads without introducing excessive mass. PLA exhibits a comparatively high specific modulus E/ρ, positioning it in the upper region of the corresponding Ashby chart and making it well suited for stiffness enhancement through material distribution. In addition, PLA offers stable and well-characterised FDM processability, particularly under ambient or non-enclosed printing conditions where thermal control is limited, enabling the fabrication of slender reinforcement features with good dimensional accuracy and repeatability without significant warping or distortion, in contrast to materials such as ABS [22]. Accordingly, PLA was selected as the stiff reinforcement material for the hybrid joint architecture.

Furthermore, the PLA–TPU material combination was selected not only based on mechanical performance, but also considering manufacturability and interfacial compatibility in dual-material FDM. For the Ultimaker S3 platform, PLA and TPU exhibit a relatively compatible printing conditions, enabling stable co-printing without complex process adjustments. This selection is further supported by the manufacturer guidelines for the Ultimaker S3 platform, which identify PLA–TPU as one of the few practically feasible dual-material combinations in terms of interfacial bonding behaviour [23].

2.4. Fabrication via dual-material FDM

The proposed hybrid PLA–TPU CRJ was fabricated using a dual-extrusion FDM printer (Ultimaker S3). The detailed printing parameters for both materials are summarised in Table 1. Process parameters were primarily based on the default Ultimaker Cura settings and subsequently adjusted to improve interfacial bonding between dissimilar materials within the hybrid joint. In particular, the extrusion temperature of TPU was increased to 235 °C when deposited adjacent to PLA regions, while active cooling was locally disabled in the interfacial zones. This strategy promotes partial re-melting and enhanced polymer diffusion at the PLA–TPU interface, thereby improving inter-material adhesion and reducing the likelihood of interfacial delamination during large elastic deformation. The internal material distribution of the hybrid joint, together with a representative fabricated specimen, is shown in Figure 4a and Figure 4b, respectively, where the PLA reinforcement ribs are shown in blue and the TPU compliant matrix is shown in black.

Table 1. Dual-extrusion FDM printing parameters for the hybrid PLA–TPU CRJ.

Parameter	Extruder 1 (PLA)	Extruder 2 (TPU 95A)
Nozzle diameter (mm)	0.25	0.4
Printing temperature (℃)	205	235
Print speed (mm/s)	40	25
Layer height (mm)	0.2	0.2
Line width (mm)	0.25	0.4
Cooling fan speed (%)	80	10
Retraction speed (mm/s)	45	45
Prime tower	Enabled	Enabled

(a) (b)

Figure 4. Fabrication of the hybrid PLA–TPU CRJ: **(a)** sectional view of the hybrid joint in Ultimaker Cura; **(b)** photograph of the fabricated hybrid PLA–TPU CRJ.

2.5. Finite element modelling and simulation methods

Finite element analysis (FEA) was employed to investigate the mechanical behaviour of the proposed diamond-shaped CRJ under different rotational loading conditions. The primary objective of the FEA simulations was not to predict absolute stiffness values with high numerical precision, but rather to enable a consistent and quantitative comparison between different material configurations and structural layouts. In particular, the simulations aimed to evaluate the influence of hybrid material distribution on on-axis compliance, off-axis stiffness, and overall directional stiffness ratios.

All simulations were conducted using the commercial finite element software ABAQUS/CAE (2024) with the implicit solver. Large-deformation effects were considered throughout the analysis to capture the nonlinear geometric behaviour inherent to CMs subjected to finite rotations. To ensure a fair comparison, all joint configurations shared identical external geometries and boundary conditions, differing only in material composition and internal structural features.

(1) Joint configurations

Three joint configurations were analysed: a mono-material PLA joint, a mono-material TPU joint, and a hybrid PLA–TPU joint, as illustrated in Figure 5a–c. In addition, a standalone PLA reinforcement rib was included as a reference configuration (Figure 5d) to characterise the intrinsic stiffness of the reinforcement element and to evaluate the effectiveness of the structural reinforcement strategy. All models shared identical external geometries (see Figure 3) to ensure that the observed differences in mechanical response were solely attributable to material distribution. The hybrid joint employed an approximate PLA-to-TPU volume ratio of 1:8, which was selected as a representative proof-of-concept configuration to demonstrate stiffness modulation through material distribution, rather than as an application-optimised design. For example, future implementations involving serially connected modular CRJ systems may require different material distributions depending on payload conditions, accumulated self-weight, and desired motion characteristics. By analysing the PLA rib independently and in combination with TPU, its standalone stiffness contribution and its synergistic effect in enhancing directional stiffness within the hybrid joint could be clearly distinguished.

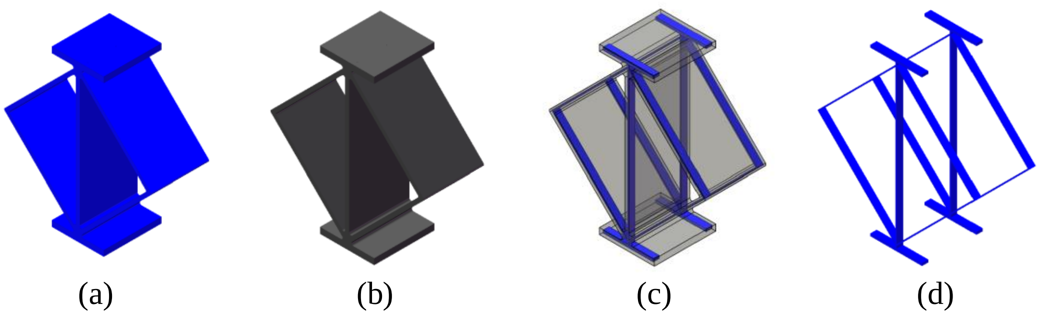

Figure 5. Diamond-shaped CRJs with different material configurations: **(a)** PLA; **(b)** TPU; **(c)** hybrid PLA-TPU; and **(d)** standalone PLA reinforcement rib.

(2) Constitutive material models

The mechanical properties of additively manufactured polymers are strongly influenced by processing parameters, including print orientation, layer height, and extrusion temperature [24]. As a result, material data reported in the literature may not accurately represent the behaviour of the FDM-printed components investigated in this study. To ensure reliable constitutive input for the FEA, experimental material characterisation was conducted using specimens fabricated with the same printer, filament, and processing parameters as the CRJ prototypes.

PLA was modelled as a homogeneous and isotropic elastic–plastic material [25], with the anisotropy induced by the layer-by-layer nature of FDM neglected, as the dominant loading and deformation directions of the joint are parallel to the printed filament layers rather than normal to the interlayer interfaces. The elastic response was defined using a linear elastic model characterised by the Young's modulus (E) and Poisson's ratio (v), followed by yielding governed by a von Mises yield criterion defined by the yield stress (σ_y). Material parameters were obtained from uniaxial tensile tests conducted on FDM-printed PLA specimens in accordance with ASTM D638 (see Appendix A). The material properties implemented in the simulations are summarised in Table 2.

Table 2. Material properties of FDM-printed PLA.

E (GPa)	v	σ_y (MPa)
2.6	0.35	53.7

TPU exhibits pronounced nonlinear elastic behaviour and was therefore modelled as a hyperelastic material [26]. In this study, the Marlow hyperelastic model implemented in ABAQUS was adopted, as it allows material characterisation based solely on uniaxial tensile test data, without requiring multi-axial experimental inputs or assuming a predefined strain energy density function [27]. The hyperelastic response of TPU was calibrated using true stress–true strain data converted from uniaxial tensile tests conducted in accordance with ASTM D412. The conversion from engineering stress–strain to true measures was performed assuming incompressible deformation, where the true strain is defined as

$$\varepsilon_{true} = \ln(1 + \varepsilon_{eng}), \tag{1}$$

and the corresponding true stress is given by

$$\sigma_{true} = \sigma_{eng}(1 + \varepsilon_{eng}), \tag{2}$$

where ε_{eng} and σ_{eng} denote the engineering strain and stress, respectively. The resulting true stress–true strain curve used for model calibration is shown in Figure 6. An isotropic material response was assumed in the hyperelastic formulation, while potential anisotropy induced by the layer-by-layer nature of the FDM process was neglected.

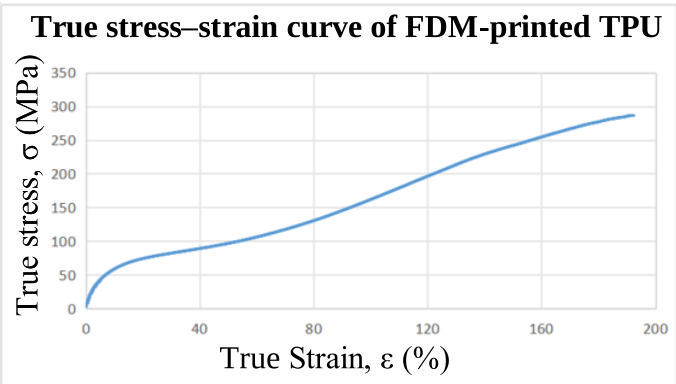

Figure 6. Hyperelastic material parameters of FDM-printed TPU derived from experimental results.

(3) Interface modelling

The interface between PLA and TPU was modelled using a surface-based cohesive behaviour formulation with a traction–separation law implemented in ABAQUS [28]. For modelling simplicity, isotropic interfacial behaviour was assumed, with identical properties assigned in the two shear directions throughout the cohesive formulation [29,30], as interfacial shear anisotropy is not a focus of this study.

The elastic response was defined by three interfacial stiffness components—normal stiffness (K_{nn}) and shear stiffnesses (K_{ss} and K_{tt})—which were treated as numerical penalty parameters and assigned to be identical in all directions. For polymer interfaces, a commonly used default value is 10^6 N/mm^2, which has been found to be sufficiently high to maintain numerical stability without introducing excessive stiffness [29]. Damage initiation was defined using a nominal stress criterion, in which the normal traction strength (t_{nn}) was obtained from uniaxial tensile tests conducted in accordance with ASTM D638 (Appendix B). Two shear traction strength components (t_{ss} and t_{tt}) were defined to correspond to the two orthogonal shear directions required by the cohesive formulation; however, both were assigned the same value based on single-lap shear tests conducted in accordance with ASTM D5868 (Appendix B).

Damage evolution was governed by an energy-based cohesive law [31]. The Mode I fracture energy (G_I) was determined from double cantilever beam (DCB) tests following ASTM D5528. Mode II and Mode III fracture energies (G_{II} and G_{III}) were defined to represent shear-dominated delamination modes and were both determined from end-notched flexure (ENF) tests following ASTM D7905, with identical values assigned for modelling simplicity. Mixed-mode fracture behaviour was described using the Benzeggagh–Kenane (BK) criterion, with the BK exponent calibrated from mixed-mode bending (MMB) procedures reported in the literature [32]. All cohesive parameters implemented in the finite element model are summarised in Table 3, with detailed experimental procedures and fracture energy calculations provided in Appendix C.

Table 3. Cohesive parameters used for modelling the PLA–TPU interface.

K_{nn} (MPa)	K_{ss} (MPa)	K_{tt} (MPa)	t_{nn} (MPa)	t_{ss} (MPa)	t_{tt} (MPa)	G_I (mJ)	G_{II} (mJ)	G_{III} (mJ)	n
1.00E + 6	1.00E + 6	1.00E + 6	5.1	6.1	6.1	72	102	102	0.9

(4) Boundary Conditions and Loading Protocol

The boundary conditions and loading protocol were designed to evaluate the on-axis rotational compliance about the z-axis (Rz), together with the off-axis rotational stiffness associated with rotations about the x- and y-axes (Rx and Ry), of the CRJ. The bottom surface of the joint was fully constrained using an *ENCASTRE* boundary condition, restricting all translational and rotational DOF. A reference point (RP) was defined at the geometric centre of the top surface, and a kinematic coupling was applied to ensure rigid-body motion of the top surface during rotational loading.

Three independent rotational loading cases were considered to evaluate the joint response about the principal and off-axis directions, as illustrated in Figure 7. For the on-axis rotation (Figure 7a), a prescribed rotation of 1.5 rad was applied about the Z-axis to assess the primary compliant motion of the joint, while rotations about the remaining axes were constrained to ensure pure axial deformation.

To assess the joint's resistance to unintended off-axis deformation, two off-axis rotational loading cases were analysed. A small rotation of 0.03 rad was applied about the X-axis (Figure 7b) to evaluate off-axis bending stiffness, with rotations about the Y- and Z-axes constrained. Similarly, a rotation of 0.03 rad was applied about the Y-axis (Figure 7c) to assess torsional stiffness and potential instability behaviour, while rotations about the X- and Z-axes were constrained.

In all loading cases, rotations about the non-loaded axes were constrained to isolate the intended deformation mode and enable a consistent comparison of rotational stiffness and deformation behaviour.

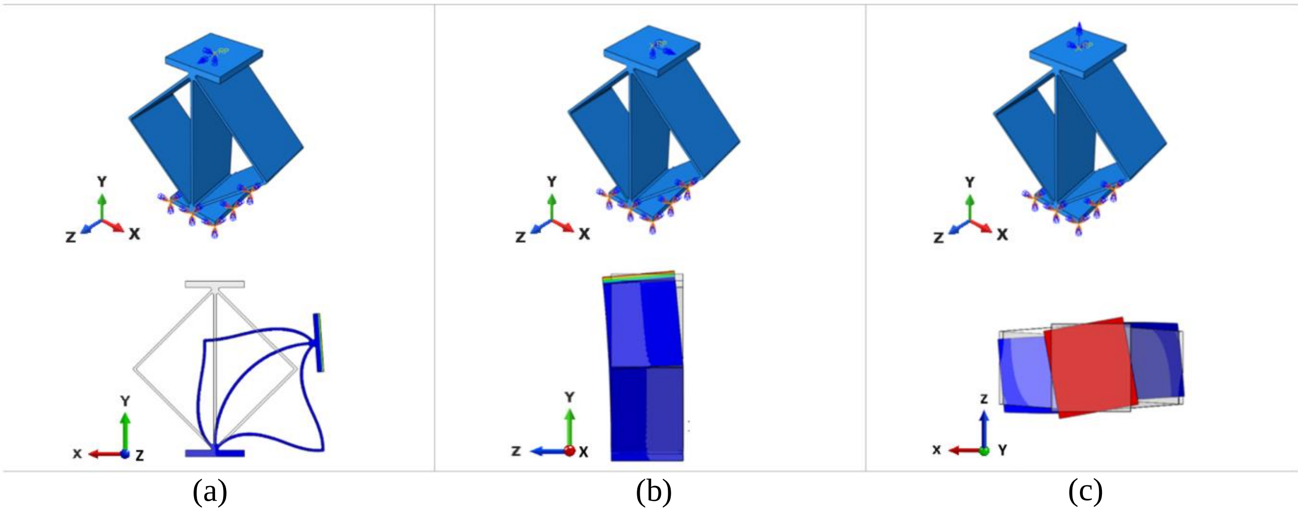

Figure 7. Boundary conditions and deformation modes of the CRJ under rotational loading: **(a)** rotation about the Z-axis; **(b)** rotation about the X-axis; and **(c)** rotation about the Y-axis.

3. Results

3.1. Directional rotational stiffness of diamond-shaped CRJs

The rotational behaviour of the diamond-shaped CRJ was evaluated under on-axis (Z-axis) and off-axis (X- and Y-axis) loading to assess directional compliance. Under a prescribed 1.5 rad rotation about the Z-axis, all joint configurations exhibited an approximately linear moment–angle relationship over the full deformation range (Figure 8a). The approximately linear moment–angle relationship observed in the present study is attributed to the symmetric diamond-shaped configuration, which does not introduce significant nonlinear effects (such as load stiffening) during the primary motion. This linear relationship is highly desirable in most engineering applications due to the simplicity of the resulting stiffness equation. To enable a clear comparison of the linear response, an enlarged view with a magnified y-axis is presented in Figure 8b. Linear regression of the enlarged responses was used to extract the on-axis rotational stiffness, showing that the PLA joint requires substantially higher actuation moments, whereas both the TPU and hybrid PLA–TPU joints achieve the same rotation with significantly lower moments, indicating enhanced on-axis compliance.

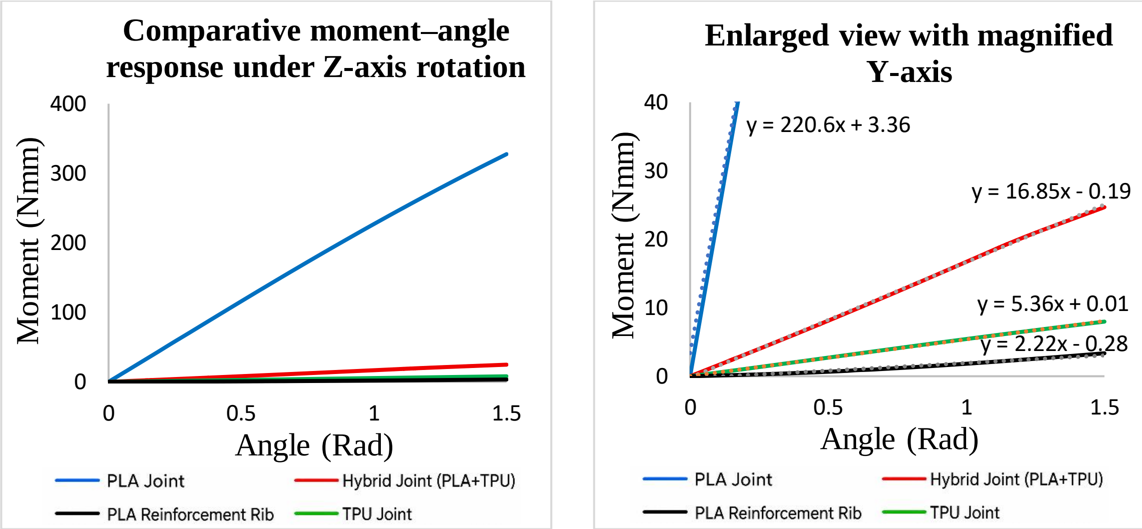

(a) (b)

Figure 8. Moment–angle response of diamond-shaped CRJs under Z-axis rotation: **(a)** full-range moment–angle curves; **(b)** enlarged view with a magnified Y-axis, showing linear regression fits used to extract on-axis rotational stiffness.

Off-axis rotational responses about the X-axis are shown in Figure 9a. The PLA and hybrid joints exhibit a rapid stiffness reduction associated with instability onset, while the TPU joint maintains a smooth, monotonic response without a distinct buckling event. As off-axis rotation is not an intended operating mode, stiffness was evaluated in the pre-instability regime at an applied moment of 30 Nmm, corresponding to the linear elastic response region (Figure 9b). Similarly, the Y-axis moment–angle curves (Figure 10a) remain approximately linear over most of the deformation range, with pronounced nonlinearity emerging only near the end in the PLA joint due to instability-related deformation. For consistent comparison, stiffness values were extracted prior to instability (Figure 10b).

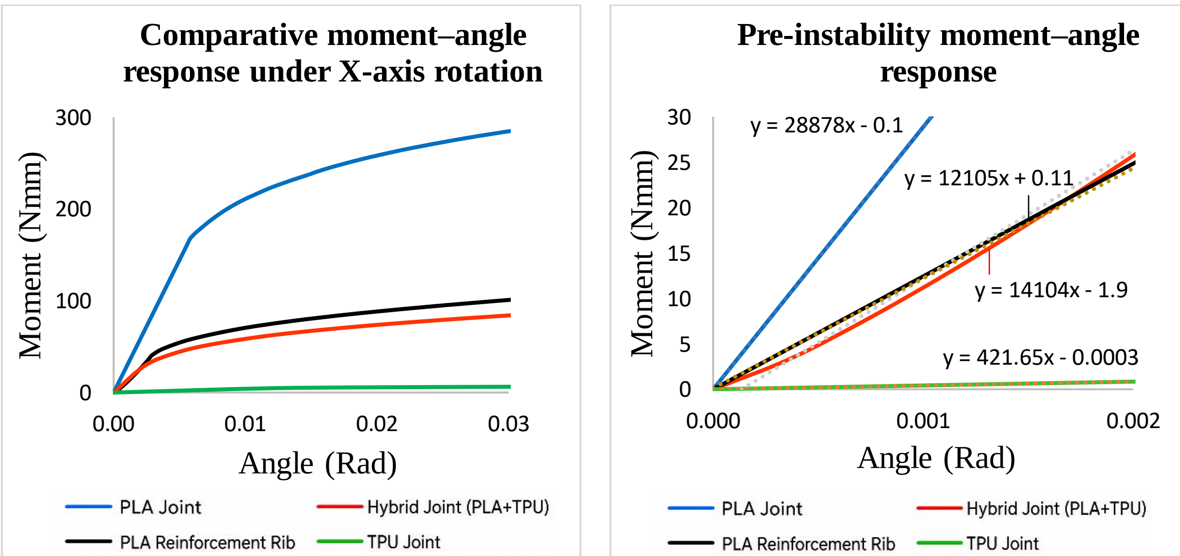

(a) (b)

Figure 9. Moment–angle response of diamond-shaped CRJs under X-axis rotation: **(a)** full response; **(b)** pre-instability regime with linear regression fits.

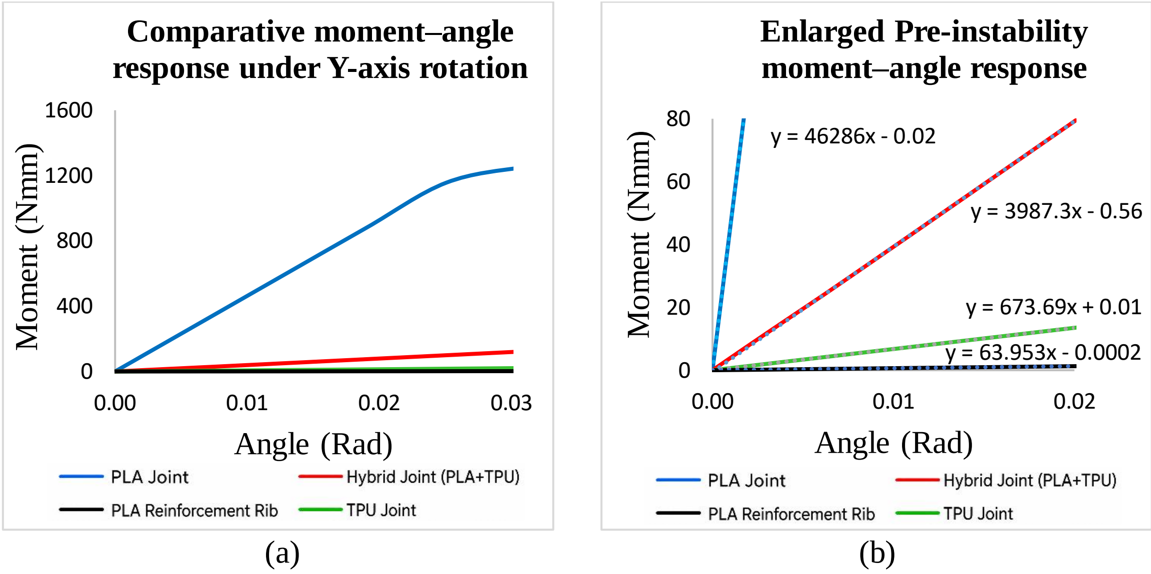

Figure 10. Moment–angle response of diamond-shaped CRJs under Y-axis rotation: **(a)** full response; **(b)** enlarged pre-instability view with linear regression fits.

Directional stiffness was quantified by normalising the off-axis stiffness values by the on-axis stiffness, yielding X/Z and Y/Z ratios (Table 4). The hybrid PLA–TPU joint exhibits the highest stiffness ratios (X/Z = 830, Y/Z = 235), indicating strong resistance to unintended off-axis rotations while retaining compliance about the intended rotational axis. In contrast, the TPU joint shows near-isotropic compliance, while the PLA joint remains stiff in all directions and therefore provides limited directional selectivity.

Table 4. Off-axis-to-on-axis rotational stiffness ratios of diamond-shaped CRJs.

Joint configuration	**Rotational stiffness about the Z-axis (N mm/rad)**	**Rotational stiffness about the X-axis (N mm/rad)**	**Rotational stiffness about the Y-axis (N mm/rad)**	**Stiffness Ratio (X/Z)**	**Stiffness Ratio (Y/Z)**
PLA Joint	221	28878	46286	131	209
TPU Joint	5	422	674	84	135
Hybrid PLA-TPU Joint	17	14104	3987	830	235

3.2. Stress response and interfacial integrity

The stress distributions under on-axis rotation about the z-axis (Rz) are shown in Figs. 11 and 12 for the hybrid and single-material configurations, respectively. The intended on-axis rotation about the z-axis (Rz) corresponds to a significantly larger rotational deformation (1.5 rad) than the off-axis rotations about the x- and y-axes (Rx and Ry), which were limited to 0.03 rad, and is therefore considered the governing loading condition. Although additional analyses were conducted for off-axis rotations, no more critical stress state or additional yielding was identified; therefore, these results are not shown for brevity.

As shown in Figure 11a, the deformation pattern of the hybrid configuration indicates coordinated bending between the compliant outer TPU skin and the embedded PLA reinforcement rib. Owing to the higher stiffness of the PLA material, the reinforcement rib experiences higher stress levels than the outer TPU skin (11.08 MPa in Figure 11b compared with 4.15 MPa in Figure 11c), suggesting that the PLA rib plays an important role in stiffness support and load transfer during rotational deformation. This behaviour is consistent with the intended I-beam-inspired design concept, in which the TPU component primarily functions as a compliant web that separates the stiffer PLA reinforcement regions, rather than acting as the main stiffness-supporting component.

As shown in Figure 12a, the single-material PLA joint reaches the highest stress levels and exhibits yielding, whereas both the TPU joint (Figure 12b) and the hybrid joint maintain substantially lower stresses. Notably, the PLA reinforcement rib embedded within the hybrid joint experiences significantly lower peak stress than the standalone PLA rib shown in Figure 12c, indicating more effective load redistribution and deformation sharing between the stiff and compliant components. The key stress results discussed above are summarised in Table 5 for comparison.

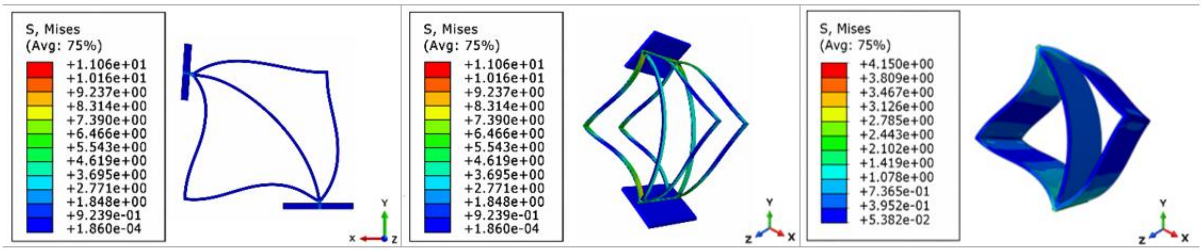

(a) (b) (c)

Figure 11. Stress distribution in the hybrid joint and its subcomponents: **(a)** hybrid joint; **(b)** PLA rib; **(c)** TPU skin.

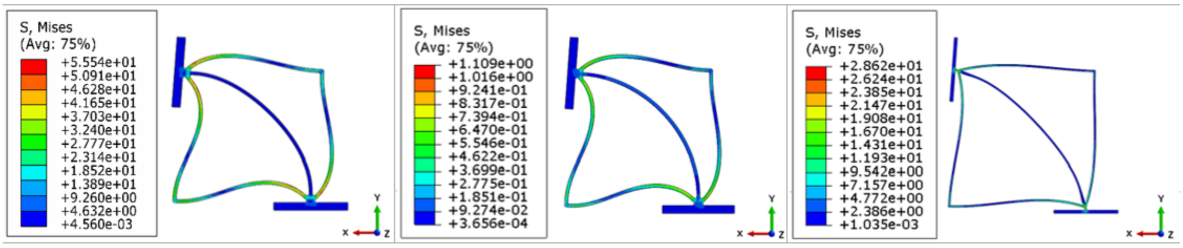

(a) (b) (c)

Figure 12. Stress distribution in single-material joints: **(a)** PLA joint; **(b)** TPU joint; **(c)** PLA rib.

Table 5. Maximum von Mises stress of joint components under Z-axis rotation (1.5 rad).

Joint configuration	Component	Maximum von Mises stress (MPa)	Yielding observed
Hybrid joint	PLA rib	11.09	No
	TPU matrix	4.15	No
TPU joint	—	1.11	No
PLA joint	—	55.54	Yes
PLA rib (standalone)	—	28.62	No

The interface simulation results indicate that interfacial damage in the hybrid joint is highly localised, occurring primarily near the rib–skin connections (see Figure 13), where the cohesive surface damage variable CSDMG approaches 1, indicating near-complete local degradation. In contrast, the majority of the bonded interface remains in a low-damage state, with CSDMG values close to zero and continues to effectively transfer load. Overall, when the hybrid PLA–TPU joint undergoes a 1.5-rad rotation about the Z-axis, its structural integrity remains high. The bonded surface effectively constrains relative slip between the two materials, promoting cooperative mechanical behaviour rather than interfacial separation.

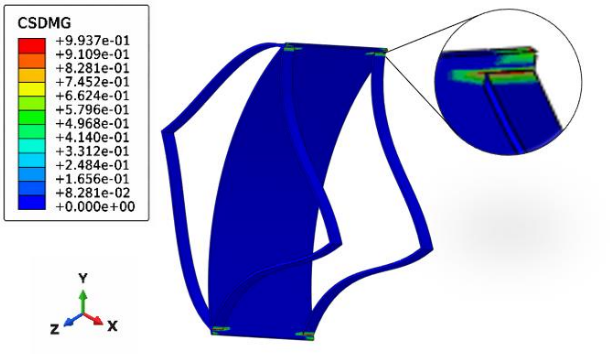

Figure 13. Damage analysis in the PLA-TPU bonded interface of the hybrid joint.

4. Conclusion

This study presented the design and numerical evaluation of a hybrid CRJ that enhances directional stiffness while maintaining large elastic rotational compliance. By integrating stiff PLA reinforcement ribs within a compliant TPU matrix, the proposed joint achieves a substantially higher off-axis to on-axis rotational stiffness ratio compared with mono-material PLA and TPU joints, demonstrating improved resistance to unintended deformation modes without compromising compliant rotation about the intended axis.

Finite element simulations show that the hybrid joint attains stiffness ratios of X / Z = 830 and Y / Z = 235 under identical geometric and loading conditions, significantly exceeding those of mono-material counterparts. Stress and interfacial damage analyses further indicate that the hybrid material architecture promotes effective load sharing between stiff and compliant components, with interfacial degradation remaining highly localised under large elastic deformation.

These results demonstrate that hybrid material distribution provides an effective joint-level strategy for addressing the stiffness–flexibility trade-off in CRJ design. Future work will focus on experimental validation of the proposed joint using improved additive manufacturing approaches (such as PolyJet) to minimise anisotropic effects and enable more consistent comparison with the numerical model. In addition, the influence of material distribution on directional stiffness will be further explored across different joint geometries, together with application-specific design optimisation to mitigate stress concentration and enhance structural performance.

Data availability statement

The data supporting the findings of this study are available in the Zenodo repository at: https://doi.org/10.5281/zenodo.18713312.

Declaration of generative AI and AI-assisted technologies

During the preparation of this manuscript, the authors used ChatGPT only for language polishing and improving readability. The authors take full responsibility for the content of the manuscript.

Acknowledgments

This research did not receive any specific grant from funding agencies in the public, commercial, or not-for-profit sectors.

Authors' contribution

Conceptualisation, Zhengyao Wang and Guangbo Hao; methodology, Zhengyao Wang, with guidance on ABAQUS finite element modelling provided by Yancheng Zhang; software and formal analysis, Zhengyao Wang; investigation and data curation, Zhengyao Wang; writing—original draft preparation, Zhengyao Wang; writing—review and editing, Zhengyao Wang, Guangbo Hao, Richard Kavanagh, and Yancheng Zhang; supervision, Guangbo Hao and Richard Kavanagh. All authors have read and agreed to the published version of the manuscript.

Conflicts of interest

Guangbo Hao holds the position of Associate Editor for *Advanced Equipment* and has not peer reviewed or made any editorial decisions for this paper.

References

[1] Howell LL, *Compliant Mechanisms*. New York: John Wiley & Sons, 2001.

[2] Brigham Young University. Compliant mechanism research group: About compliant mechanisms. Available: https://compliantmechanisms.byu.edu/about-compliant-mechanisms (accessed on 11 April 2025).

[3] Palmieri G, Palpacelli MC, Callegari M. Study of a fully compliant U-joint designed for minirobotics applications. *ASME J. Mech. Des.* 2012, 134(11):111003.

[4] Russo M, Sadati SMH, Dong X, Mohammad A, Walker ID, *et al.* Continuum robots: an overview. *Adv. Intell. Syst.* 2023, 5:2200367.

[5] Li S, Hao G. Current trends and prospects in compliant continuum robots: a survey. *Actuators* 2021, 10(7):145.

[6] Koese B. Design of a large stroke two DoF translation stage based on compliant joints. Master's Thesis, Eindhoven University of Technology, 2021.

[7] Lobontiu N. *Compliant Mechanisms: Design of Flexure Hinges*. Boca Raton: CRC Press, 2002.

[8] Merriam EG. Stiffness reduction strategies for additively manufactured compliant mechanisms. dissertation, Brigham Young University, 2016.

[9] Li G, Yu J, Tang Y, Pan J, Cao S, *et al.* Design and modeling of continuum robot based on virtual-center of motion mechanism. *Front. Mech. Eng.* 2023, 18(2):23.

[10] Li S, Hao G, Wright WMD. Design and modelling of an anti-buckling compliant universal joint with a compact configuration. *Mech. Mach. Theory* 2021, 156:104162.

[11] Dewi PT, Rao P, Burgner-Kahrs J. A lightweight modular segment design for tendon-driven continuum robots with pre-programmable stiffness. In *Proceedings of the 2024 IEEE 7th International Conference on Soft Robotics (RoboSoft)*, San Diego, USA, 2024, pp. 531–536.

[12] Kabganian M, Ghasemi A, Mirsalim MM. Towards design optimization of compliant mechanisms. *Mech. Mach. Theory* 2024, 196:105593.

[13] Ling M, Zhang X, Tian Y. Compliance and precision modeling of general notch flexure hinges. *Precis. Eng*. 2023, 82:36–49.

[14] Wang X, Yu Y, Xu Z, Xu A, Qin C. Modelling and performance analysis of a curvature-adjustable multiple-axis flexure hinge based on Bézier curve. *Proc. Inst. Mech. Eng., Part C: J. Mech. Eng. Sci.* 2024; 238(9):3710-3723.

[15] Farhadi Machekposhti D, Tolou N, Herder JL. A review on compliant joints and rigid-body constant velocity universal joints toward the design of compliant homokinetic couplings. *J. Mech. Des*. 2015, 137(3):032301.

[16] Zhu J, Hao G, Liu T, Li H, Design of an over-constraint based nearly-constant amplification ratio compliant mechanism. Mech. Mach. Theory 2023, 186:105347.

[17] Li H, Chen W, Yi L, Leng C, Wu H. Design, modeling and manufacture error identification of a new 6-degree-of-freedom (6-DOF) compliant parallel manipulator. *Mech. Sci.* 2025, 16(1):143–156.

[18] Sun Y, Liu Y, Lueth T. Optimization of stress distribution in tendon-driven continuum robots using fish-tail-inspired method. *IEEE Robot. Autom. Lett.* 2022, 7(2):3380–3387.

[19] Meyer P, Zentner L, Otter M. Test methods for the mechanical characterization of flexure hinges. *Exp. Mech*. 2023, 63:987–1002.

[20] Gere JM, Goodno BJ. *Mechanics of Materials*, 7th ed. Toronto: Cengage Learning, 2010.

[21] Ashby MF. *Materials Selection in Mechanical Design*, 2nd ed. Boston: Butterworth-Heinemann, 2010.

[22] Kantaros A, Katsantoni M, Ganetsos T, Petrescu N. The evolution of thermoplastic raw materials in high-speed FFF/FDM 3D printing era: Challenges and opportunities. *Materials* 2025, 18(6):1220.

[23] Ultimaker. UltiMaker 3 - Material compatibility. Available: https://support.makerbot.com/s/article/1667411318161 (accessed on 15 October 2025).

[24] Mencarelli M, Sisella M, Puggelli L, Innocenti B, Volpe Y. Sensitivity analysis of 3D printing parameters on mechanical properties of fused deposition modeling-printed polylactic acid parts. *Appl. Mech.* 2025, 6(1):1.

[25] Farah S, Anderson DG, Langer R. Physical and mechanical properties of PLA, and their functions in widespread applications—a comprehensive review. *Adv. Drug Delivery Rev.* 2016, 107:367–392.

[26] Martin DJ, Osman AF, Andriani Y, Edwards GA. Thermoplastic polyurethane (TPU)-based polymer nanocomposites. In *Advances in Polymer Nanocomposites*. Cambridge: Woodhead Publishing, 2012. pp. 321–350.

[27] Du T, Sun L, Wan J. A worm-like crawling soft robot with pneumatic actuators based on selective laser sintering of TPU powder. *Biomimetics* 2022, 7(4):205.

[28] Park K, Choi H, Paulino GH. Assessment of cohesive traction–separation relationships in ABAQUS: a comparative study. *Mech. Res. Commun.* 2016, 78:71–78.

[29] Lu X, Ridha M, Chen BY, Tan VBC, Tay TE. On cohesive element parameters and delamination modelling. *Eng. Fract. Mech.* 2019, 206:278–296.

[30] van Tonder JD, Venter MP, Venter G. A novel method for resolving non-unique solutions observed in fitting parameters to the Mooney Rivlin material model. *Finite Elem. Anal. Des.* 2023, 225:104006

[31] Johar M, Wong KJ, Tamin N. Mixed-mode delamination failures of quasi-isotropic quasi-homogeneous carbon/epoxy laminated composite. In *Laminated Composite Materials*. London: IntechOpen, 2017.

[32] Benzeggagh ML, Kenane M. Measurement of mixed-mode delamination fracture toughness of unidirectional glass/epoxy composites with mixed-mode bending apparatus. *Compos. Sci. Technol.* 1996, 56(4):439–449.